Journal of Hydrology 542 (2016) 541–551

Contents lists available at ScienceDirect

Journal of Hydrology

journal homepage: www.elsevier.com/locate/jhydrol

Research papers

Representativeness of 2D models to simulate 3D unstable variable density flow in porous media

Bastian Knorr [a,b], Yueqing Xie [b,*], Christine Stumpp [a], Piotr Maloszewski [a,c], Craig T. Simmons [b]

[a] Institute of Groundwater Ecology, Helmholtz Zentrum München, German Research Center for Environmental Health (GmbH), Ingolstaedter Landstr. 1, 85764 Neuherberg, Germany
[b] School of the Environment & National Centre for Groundwater Research and Training, Flinders University, Adelaide, South Australia, Australia
[c] AGH University of Science and Technology, Department of Hydrogeology and Engineering Geology, Al. Mickiewicza 30, 30-059 Kraków, Poland

ARTICLE INFO

Article history:
Received 1 March 2016
Received in revised form 29 August 2016
Accepted 9 September 2016
Available online 14 September 2016
This manuscript was handled by P. Kitanidis, Editor-in-Chief, with the assistance of Jian Luo, Associate Editor

Keywords:
Variable density flow
Porous media
Column experiments
Numerical modelling

ABSTRACT

Variable density flow in porous media has been studied primarily using numerical models because it is a semi-chaotic and transient process. Most of these studies have been 2D, owing to the computational restrictions on 3D simulations, and the ability to observe variable density flow in 2D experimentation. However, it is recognised that variable density flow is a three-dimensional process. A 3D system may cause weaker variable density flow than a 2D system due to stronger dispersion, but may also result in bigger fingers and hence stronger variable density flow because of more space for fingers to coalesce. This study aimed to determine the representativeness of 2D modelling to simulate 3D variable density flow. 3D homogeneous sand column experiments were conducted at three different water flow velocities with three different bromide tracer solutions mixed with methanol resulting in different density ratios. Both 2D axisymmetric and 3D numerical simulations were performed to reproduce experimental data. Experimental results showed that the magnitude of variable density flow increases with decreasing flow rates and decreasing density ratios. The shapes of the observed breakthrough curves differed significantly from those produced by 2D axisymmetric and 3D simulations. Compared to 2D simulations, the onset of instabilities was delayed but the growth was more pronounced in 3D simulations. Despite this difference, both 2D axisymmetric and 3D models successfully simulated mass recovery with high efficiency (between 77% and 99%). This study indicates that 2D simulations are sufficient to understand integrated features of variable density flow in homogeneous sand column experiments.

1. Introduction

Density driven flow is an essential process for describing solute transport in porous and fractured systems where fluid flow is driven by a variation in density. Variations in density can be caused by solute concentration, temperature and/or pressure of a fluid (Simmons, 2005; Simmons et al., 2001). In particular, this density driven flow is of strong relevance to practical issues including salt water intrusion (Huyakorn et al., 1987; Pinder and Cooper, 1970; Van Dam et al., 2009; Voss and Souza, 1987), contaminant transport (Frind, 1982; Oostrom et al., 1992a, 1992b; Schincariol and Schwartz, 1990), contamination site remediation (Flowers and Hunt, 2007) and nuclear waste disposal (Hassanizadeh and Leijnse, 1988; Herbert et al., 1988). Depending on several factors (i.e., porous medium permeability, porosity, water flow velocity and density ratio of intruding fluid to ambient groundwater), density driven flow can become unstable under certain circumstances (Biggar and Nielsen, 1964; Krupp and Elrick, 1969; Rose and Passioura, 1971). Unstable density driven flow is characterised by the formation of finger-shaped instabilities with density constantly varying in space and time. This unstable density driven flow (or variable density flow) is superimposed onto regional groundwater flow and hence can cause more widespread aquifer contamination by distributing contaminants vertically (Beinhorn et al., 2005; Flowers and Hunt, 2007). Being able to reliably understand, observe, measure, simulate and predict variable density flow is a critical challenge for hydrogeology (Simmons, 2005).

Variable density flow has been studied primarily through 2D settings to investigate onset, growth and decay of instabilities (e.g., Voss and Souza, 1987; Xie et al., 2010, 2011, 2012; Riaz et al., 2006; Jang and Aral, 2007; Prasad and Simmons, 2003, 2005). The implicit assumption of 2D studies is that mixing is not important in the direction orthogonal to the 2D planes and that a 2D transect is representative of a 3D system. Although this assumption is not valid in the real world, most studies have

* Corresponding author.
E-mail address: yueqing.xie@flinders.edu.au (Y. Xie).

http://dx.doi.org/10.1016/j.jhydrol.2016.09.026
0022-1694/

nevertheless adopted it for simplicity. There has been little attempt to test, justify and discuss the assumptions made with respect to dimensionality and the effects it may have on flow and transport behaviour and model results. For example, Xie et al. (2010) modified the classic 2D Elder problem to examine the effect of time-varying salt loading on variable density flow. Riaz et al. (2006) performed 2D numerical modelling to verify predictions about instability onset time made by linear stability analysis in the context of carbon dioxide sequestration within saline aquifers. Van Dam et al. (2009) established several 2D transects to capture salty fingers using geophysical methods. Simmons et al. (2002) and Post and Simmons (2010) used the same 2D sand tank to investigate the fingering process in a variable saturated setting and a heterogeneous setting, respectively. Those lab and field studies have also been reproduced in 2D numerical models (Cremer and Graf, 2015; Dam et al., 2014; Post and Simmons, 2010). However, as shown by these 2D numerical studies, precise reproduction of field and experimental observations is hard due to the transient and semi-chaotic nature of variable density flow. van Reeuwijk et al. (2009) demonstrated that the classic Elder problem – a typical variable density flow system – is characterised by multiple steady state solutions. Despite this inherent issue in variable density flow, prior 2D numerical modelling studies have also indicated that reliable predictions of variable density flow can still be made if we use macroscopic features such as integrated solute mass flux, total solute mass and centre of gravity (Prasad and Simmons, 2003, 2005; Xie et al., 2012). These studies still remain 2D studies, with 2D representations of 3D realities.

3D studies are challenging and hence rare because they create increased computational burden in a numerical study and fingering patterns are challenging to visualise in an experimental setting. However, it is well recognised that variable density flow occurs in three dimensions (Diersch and Kolditz, 1998; Johannsen et al., 2006; Oswald et al., 1997; Pau et al., 2010). Both Oswald et al. (1997) and Johannsen et al. (2006) have attempted to reproduce experimental results with 3D numerical simulations. Oswald et al. (1997) found that the growth speed was reproduced correctly but the onset of instabilities was delayed in the 3D simulations. Johannsen et al. (2006) found that a detailed reproduction of observed fingering processes in the Salt Pool Problem (Oswald and Kinzelbach, 2004) cannot be obtained in the 3D simulations due to uncertainties in initial conditions and numerical errors. In addition, Diersch and Kolditz (1998) and Pau et al. (2010) simulated variable density flow in different settings only using 2D and 3D numerical models. Diersch and Kolditz (1998) extended the 2D Elder Problem to 3D. They observed similar upwelling salinity patterns in the centre of the model domain in both 2D and 3D scenarios. In the simulations of CO_2 sequestration, Pau et al. (2010) reported that the onset time of instabilities was shorter and the magnitude of the stabilized CO_2 flux was higher in 3D than in 2D. However, they argued that these differences are moderate in comparison to heterogeneities which can be normally found in geological media.

Although 3D studies do appear to become a little more common, there has not been a systematic comparison between lab or field observations, 2D and 3D numerical simulations on variable density flow. In comparison to 2D, a 3D system allows solute to migrate freely in all directions. On one hand, this freedom may result in stronger dispersion and possibly weaker variable density flow. On the other hand, it is also likely that fingers may grow bigger and so penetrate faster under gravitational influence in a 3D system. Whether 3D behaviour and modelling promotes or suppresses fingering process in mixed convective systems compared to 2D counterparts has not been examined yet.

In this study, we attempted to replicate observations in 3D lab experiments using both 2D axisymmetric and 3D numerical models. The objectives were to semi-quantitatively compare processes in 2D axisymmetric and 3D settings and also thoroughly examine the ability of 2D axisymmetric models to represent physical processes in 3D. We based this comparison on tracer experiments conducted in saturated homogeneous sand columns at three different water flow velocities and three different density ratios.

2. Material and methods

In this study a Darcy column with a diameter of 4.8 cm and a length of 50.8 cm was used to perform experiments (Fig. 1). The porous medium in the column was comprised of coarse quartz sand (Dorsilit Nr. 5F, Quarzsande GmbH, Germany) with a particle size distribution between 1.0 mm and 1.8 mm, a porosity of $n = 0.44$ and a hydraulic conductivity of $k = 7.0 \cdot 10^{-3}$ m s^{-1} (605 m d^{-1}) determined with the constant head method (Klute and Dirksen, 1986). A thin layer of silicon adhesive was implemented between the column and the coarse sand to eliminate potential preferential flow paths along the column wall. The column was packed with the coarse sand under saturated conditions to avoid entrapped air bubbles. All experiments were run with deionized and filtered water (MilliQ, MilliporeElix + Milli-Q Advantage 10A, USA) constantly flowing from the bottom to the top using a peristaltic pump (Gilson Abimed Minipuls 3). A radial-distribution device was used to inject the inflow water evenly over the whole cross section of the column. The accuracy of the peristaltic pump was ±0.2 mL h^{-1}.

Bromide is known to be free of sorption (Levy and Chambers, 1987; Maloszewski et al., 1999) and was therefore used as a conservative tracer. Potassium bromide was dissolved in the deionized and filtered water to create a bromide solution with a concentration of 95 mg L^{-1}. This very low concentration did not significantly change the fluid density and so the fresh water density could be

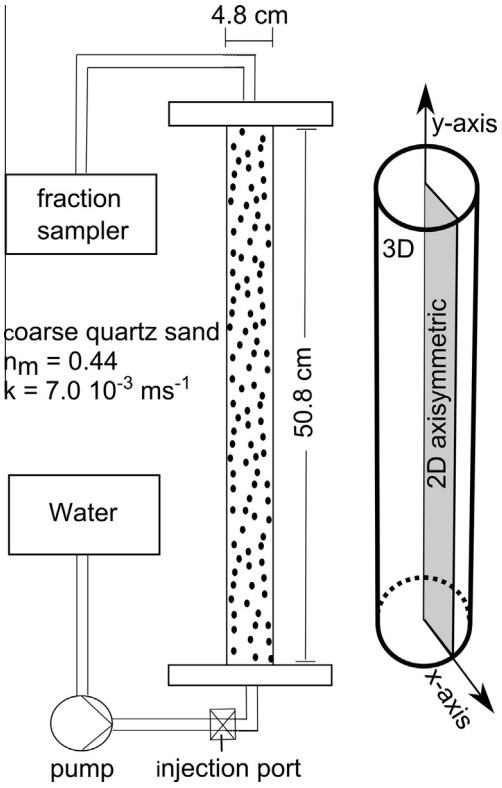

Fig. 1. Experimental design of the homogenous sand column and numerical model setup in 3D and 2D axisymmetric projection.

used to represent the density of the bromide solution. In order to perform experiments with varying levels of density-driven flow, different amounts of methanol (2% and 4% in this study) were dissolved in the bromide solution to create different fluid densities. The density ratio of the difference in density between a tracer solution (combined bromide/methanol solution) and the ambient water is a useful indicator for variable density flow:

$$\Delta\rho = \frac{(\rho_{tracer} - \rho_{water})}{\rho_{water}} \quad (1)$$

where ρ_{tracer} is the density of the injected tracer solution [M L^{-3}] and ρ_{water} is the density of the ambient water in the column [M L^{-3}]. The density of a tracer solution was calculated according to Mikhail and Kimel (1961). As a result, the addition of 2% and 4% methanol to the bromide solution resulted in $\Delta\rho = -0.0036$ and $\Delta\rho = -0.0071$, respectively. A negative $\Delta\rho$ indicates that the density of the injected tracer solution is lower than that of the ambient water. The tracer solution was injected in a short pulse (Dirac-Impulse) across the whole inlet at the bottom of the column. Density-driven flow of the light tracer cloud is aligned with the general water flow direction from the bottom to the top of the column (Fig. 1). This scenario is similar to an experimental design with heavy plumes injected at the top and a water flow direction from the top to the bottom of the column (Wood et al., 2004).

In total, three sets of tracer experiments were performed at flow rates of 30, 15 and 7.5 mL h^{-1} (i.e., water flow velocities of 1.0, 0.5 and 0.25 m d^{-1}), respectively. A summary of the experimental conditions and the densities of the tracer solutions are given in Table 1. These flow rates create background advective flow. The breakthrough curves at $\Delta\rho = 0$ were used to validate experimental setup and numerical models, and to indicate density effects by comparing to the corresponding breakthrough curves at other $\Delta\rho$. At each flow rate three experiments were conducted with the tracer solution with $\Delta\rho = 0$, -0.0036 and -0.0071. The three sets of experiments conducted at differing injection speeds of 1.0, 0.5 and 0.25 m d^{-1} are referred to as experiments A, B and C, respectively. The three groups of experiments, conducted at different injection fluid densities with $\Delta\rho = 0$, -0.0036 and -0.0071 are referred to as 0, 2 and 4, respectively. A 9 mL water sample was collected at the column outlet (top) by an auto sampler (Ma Ron GmbH, Model LF10 5M) every 0.5, 1.0 and 2.0 h for experiments A, B and C, respectively. The bromide concentration of the samples was analysed with an ion chromatograph (Dinonex 500, Dinoex, Sunnyvale, California, USA). Measured concentrations were plotted versus time to create breakthrough curves (BTCs).

In order to obtain a visual sense of variable density flow and to prove that it is a relevant process under investigated conditions, two dye tracer experiments using patent blue V (VWR International, Leuven, Belgium) were conducted at the flow rate of 15 mL h^{-1} with $\Delta\rho$ of 0.0 and -0.0071, respectively. The shapes of visible tracer front along the transparent column wall were marked in regular time intervals (once every 2 h). Patent blue V is not a conservative tracer. Sorption studies with similar dyes (Brilliant Blue) showed that they are retarded by a factor of 1.2 in soils in comparison to iodide (Flury and Flühler, 1995). However, adsorption onto quartz is unlikely since both Patent blue V and quartz are negatively charged at pH investigated in this study. Therefore, the dye is sufficient to visualise variable density flow in the applied setup.

3. Numerical modelling

In this study, the finite-element groundwater numerical simulator FEFLOW (Diersch, 2013) was employed to conduct all the simulations. FEFLOW uses the density-corrected fluid mass conservation equation and momentum conversation equation to simulate groundwater flow, and the advection-dispersion equation to simulate solute transport. A simple linear function is adopted to correlate fluid density and solute concentration. The reader is referred to Diersch (2013) for a detailed description of numerical implementation.

3.1. Model setup

Experimental results were simulated both in 2D axisymmetric and in 3D models (Fig. 1). The 3D model had the same dimensions as the experimental setup (length of 50.8 cm, diameter of 4.8 cm), whereas the 2D axisymmetric model only attempted to represent an axisymmetric cross section with the model width equal to half of the diameter (2.4 cm). A 2D axisymmetric model rather than a 2D planar model was chosen to represent the cylindrical geometry of the column. Although the 2D axisymmetric model is a representation of the 3D setting, simulations are still performed in the 2D framework and hence a plume can only migrate along the 2D cross section same as the 2D planar model. The advantage of using the 2D axisymmetric model is that results produced are directly comparable to those from 3D (i.e., mass flux units are the same). In total, 9 scenarios were examined for 2D axisymmetric and 3D models, respectively, to compare results in different combinations of flow conditions and density differences and to identify the ability of both model setups to replicate 3D variable density flow.

For both the 2D axisymmetric and the 3D models, the fluid flux boundary condition was assigned to the inlet (bottom) and the outlet (top) of the model in order to create an initially constant flow field, identical to the experiments. The assignment of the fluid flux boundary condition was used to ensure that the volume into and out of the model would not be affected by dense fluid, which could impede fluid flow near boundaries if hydraulic head boundary

Table 1
Experimental conditions (water flow velocities: A = 1.0 m d^{-1}, B = 0.5 m d^{-1}, C = 0.25 m d^{-1} and density ratios $\Delta\rho = 0$ (0), $\Delta\rho = -0.0036$ (2), $\Delta\rho = -0.0071$ (4)) and fitted parameter for numerical 2D axisymmetric and 3D simulations. α_L, k and n are fitted results. α_T is assumed to be 1/10 of α_L.

Parameter	$\Delta\rho = 0$			$\Delta\rho = -0.0036$			$\Delta\rho = -0.0071$		
	A0	B0	C0	A2	B2	C2	A4	B4	C4
Flow rate, Q (mL h^{-1})	36.8	18.6	9.2	35.6	18.0	8.9	35.9	18.5	8.8
Water flow velocity, v (m d^{-1})	1.00	0.50	0.25	1.00	0.50	0.25	1.00	0.50	0.25
Mixed convective ratio (–)	0	0	0	8.6	22.6	58.3	22.8	47.3	69.3
Rayleigh number (–)	0	0	0	4912	11,778	31,312	13,079	27,550	30,716
Tracer mass, M (mg)	0.24	0.24	0.24	0.24	0.24	0.28	0.24	0.24	0.24
Fluid flux, BC (m d^{-1})	0.49	0.25	0.12	0.47	0.24	0.12	0.48	0.24	0.12
Mass flux, BC (g m^{-2} d^{-1})	46.34	23.44	11.62	44.82	22.64	11.27	45.22	23.27	11.13
Longitudinal dispersivity, α_L (mm)	0.8	0.8	0.6	0.8	0.8	0.6	0.8	0.7	0.8
Transversal dispersivity, α_T (mm)	0.08	0.08	0.06	0.08	0.08	0.06	0.08	0.07	0.08
Hydraulic conductivity, k (m d^{-1})	605	605	605	1000	1300	1700	1350	1400	1000
Porosity, n (–)	0.435	0.435	0.430	0.420	0.415	0.420	0.420	0.420	0.410

conditions were used. A time-varying mass flux boundary condition was imposed onto the inlet of a model to mimic the pulse of tracer injection. The outlet of the model was set with the default zero-concentration-gradient boundary condition. Because of the fluid flux boundary condition, the divergence form of the transport equation was selected to account for both advection and dispersion through the bottom boundary. Detailed fluid flux and mass flux values are given in Table 1.

Both models were discretised to ensure that the grid Peclet number does not exceed 2.0 (Diersch and Kolditz, 2002). Rühle et al. (2013) and Kanel et al. (2008) estimated longitudinal dispersivities of 1.54 mm and 1.0 mm, respectively, for porous media with similar grain size distributions and travel lengths to this study. Hence, the grid sizes of the 2D axisymmetric and 3D models in the longitudinal direction need to be smaller than 2.0 mm. Given the geometric difference between 2D axisymmetric and 3D models, exactly the same grid discretisation was impossible. The 2D axisymmetric model resulted in 28,310 quadrilateral elements with the same lateral and vertical grid sizes (0.63 mm) i.e., square elements. The 3D model generated 922,020 elements with a vertical grid size 0.8 mm and an average lateral grid size 1.7 mm (triangular elements across a horizontal plane). The lateral grid size was larger in 3D than 2D axisymmetric due to computational restriction. As variable density flow occurs predominantly in the vertical direction, this difference in lateral grid sizes did not have a significant impact on dense fluid migration. In both models, the second-order predictor–corrector scheme (AB/TR) was used to automatically determine time steps based on errors with the initial time step lower than $1 \cdot 10^{-7}$ min. The maximum time step of 1 min and the maximum growth factor of 1.01 were imposed to restrict time steps to ensure model convergence.

3.2. Model simulation and quantification

In this study, flow and transport parameters (hydraulic conductivity k, porosity n and longitudinal dispersivity α_L) were fitted by a trial and error method. The diffusion coefficient for bromide ($D_0 = 1.5 \cdot 10^{-9}$ m^2 s^{-1}) was taken from Małloszewski and Zuber (1992). Viscosity was assumed to be constant at 10^{-3} kg (m s)$^{-1}$. Since homogenous and uniform quartz sand was used, anisotropy in hydraulic conductivity can be neglected. Transverse dispersivity (α_T) was assumed to be 1/10 of α_L (Zheng and Bennett, 1995). Parameters estimated in 2D axisymmetric were then used to run simulations in 3D.

It should be noted that although k and n were directly determined in the lab in context of this study, these parameters were still allowed to vary within a factor of 3 for data fitting. Simmons et al. (2002) showed that the determination of k using different methods can have an uncertainty of a factor of approximately 3. Longitudinal dispersivity cannot be determined directly. In the fitting procedure it was allowed to vary in the same range as found by other researchers for similar sediments and travel distances (Kanel et al., 2008; Rühle et al., 2013).

Two quantitative diagnostics were used to evaluate the performance of numerical models and included mean concentration of outflow and relative recovery rate of mass. The mean concentration at a specific time *t* was computed by dividing volumetric mass flux by volumetric fluid flux, as given by

$$C(t) = \sum_{k=1}^{n} C_{tk} S_{tk} q_{tk} \Big/ \sum_{k=1}^{n} S_{tk} q_{tk} \tag{2}$$

where C_{tk} is the concentration of the node k at time t [M L^{-3}], q_{tk} is the Darcy velocity of the node k at time t [L T^{-1}]; S_{tk} is the area surrounding node k [L^2]. In variable density flow, concentration is not uniform across the outflow face. This method provides the closest mean concentration to an actual experimental measurement made when a sample was fully mixed. Relative recovery rates RR(t) were calculated for both fitted curves and experimental data (Maloszewski and Zuber, 1990):

$$RR(t) = \frac{Q}{M} \int_0^t C(t)dt \tag{3}$$

where M is the total mass of the injected tracer [M]; Q is the volumetric flow rate [L^3 T^{-1}] and C(t) is either the observed or modelled concentration [M L^{-3}]. For numerical modelling, Q equals $\sum_{i=1}^{n} S_{ti} q_{ti}$. It is expected that RR(t) is less variable and more predictable than C (t) as the total mass is the mass accumulated over time.

The goodness of fitting was used as a quantitative measure given by (Hornberger et al., 1992):

$$ME = \left[1 - \frac{\sum_{i=1}^{N} (C_f^i - C_{obs}^i)^2}{\sum_{i=1}^{N} (C_{obs}^i - C_{mean})^2}\right] \cdot 100\% \tag{4}$$

$$C_{mean} = \frac{\sum_{i=1}^{N} C_{obs}^i}{N} \tag{5}$$

where ME is the model efficiency [–], C_{obs}^i is the observed concentration [M L^{-3}] at time t_i [T], C_f^i is the fitted concentration [M L^{-3}] at time t_i [T], C_{mean} is the mean value of observed concentrations [M L^{-3}] and N is the number of observations [–]. Similar to Eqs. (4) and (5), the efficiency of model relative mass recovery was calculated as:

$$MME = \left[1 - \frac{\sum_{i=1}^{N} (RR_f^i - RR_{obs}^i)^2}{\sum_{i=1}^{N} (RR_{obs}^i - RR_{mean})^2}\right] \cdot 100\% \tag{6}$$

$$RR_{mean} = \frac{\sum_{i=1}^{N} RR_{obs}^i}{N} \tag{7}$$

where MME is the mass model efficiency [–], RR_{obs}^i is the observed relative mass recovery [–] at time t_i [T], RR_f^i is the relative mass recovery [–] at time t_i [T], RR_{mean} is the mean value of relative mass recovery [–] and N is the number of observations [–].

4. Experimental and modelling results

4.1. Observed tracer breakthrough curves

The comparison of two dye tracer experiments shows qualitatively the effect of the density ratio ($\Delta\rho$) on fluid flow and solute transport in the sand column (Fig. 2). When $\Delta\rho = 0$, observable tracer fronts were relatively uniform on the column wall (Fig. 2A). The migration speed of the tracer was consistent with the water flow velocity. This indicates that the applied dye tracer behaved conservatively when the density effect was absent. When $\Delta\rho = -0.0071$, wavy tracer fronts were observed (Fig. 2B) in accord with unstable density driven flow. It can be seen that at least three fingers were developed. One finger was growing stronger and moving faster than the other two. In 6 h, the tracer front of the largest finger had moved to 22 cm, whereas the tracer fronts of the other two fingers were at 18 cm. The migration speed of the tracer in all three fingers was about 1.5–2 times greater than the water flow velocity. Clearly, the density of the intruding fluid accelerated the tracer migration in the porous medium.

Observed concentrations were plotted versus porewater volume for each experiment (Fig. 3). A summary of experimental conditions and parameters is given in Table 1. The injected bromide mass was recovered in every experiment indicated by the averaged relative mass recovery of 98 ± 5%. Ideally, the mass recovery for an

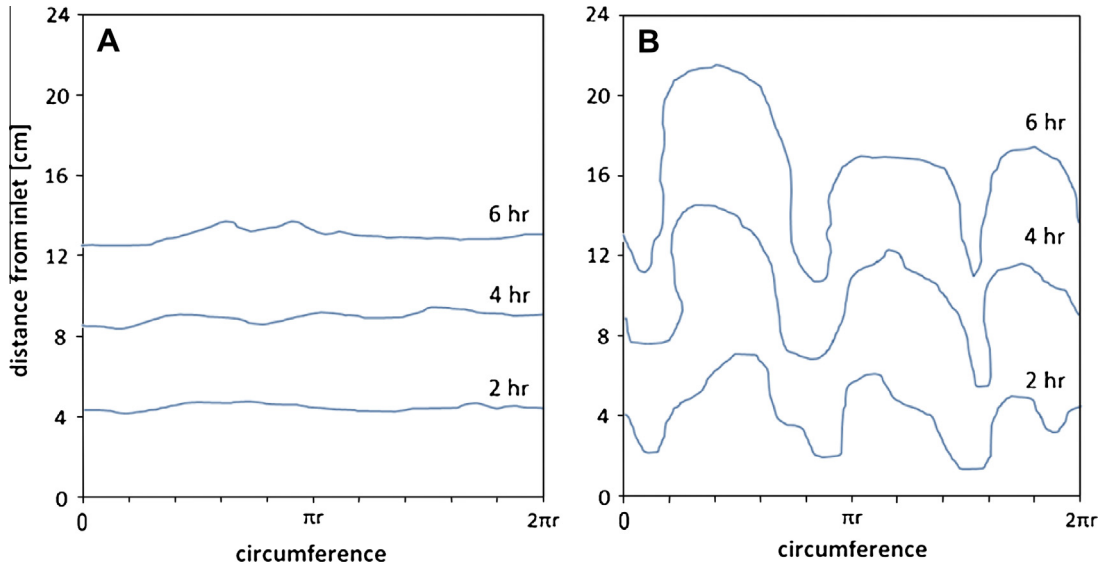

Fig. 2. Tracer fronts observed at the transparent column wall after 2 h, 4 h and 6 h in dye tracer experiments with different density ratios, (A) $\Delta\rho = 0$ and (B) $\Delta\rho = -0.0071$. The flow rate was 15 mL h^{-1} in both experiments (water flow velocity 0.5 m d^{-1}).

ideal tracer in a closed system should be 100%. However, lower and higher values can be observed due to cumulative errors caused by analytics and the measurement of the outflow. Experiments A0, B0, and C0 ($\Delta\rho = 0$) produced nearly symmetrical BTCs regardless of water flow velocities. This indicates that no artefacts such as tailings and double peaks are caused by errors in the experimental setup. In all the experiments using tracers with non-zero $\Delta\rho$, observed divergences from the symmetric BTCs were caused by variable density flow. As expected, variable density flow increased with decreasing water flow velocity and decreasing density ratio (Biggar and Nielsen, 1964; Krupp and Elrick, 1969; Rose and Passioura, 1971; Wood et al., 2004). This can be explained by an increasing ratio of the flow driven by a density gradient to the flow driven by a hydraulic gradient (mixed convection ratio). The influence of density on the tracer transport is demonstrated in Fig. 3A where concentrations of experiments conducted at 0.5 m d^{-1} are plotted versus cumulative outflow divided by volume of total mobile water (pore volume). The first peak of the observed BTCs appeared after 0.99, 0.93 and 0.75 pore volumes at $\Delta\rho = 0$, $\Delta\rho = -0.0036$ and $\Delta\rho = -0.0071$, respectively. A decrease in $\Delta\rho$ from 0 to −0.0036 caused a lower peak concentration (15%), earlier arrival of the peak (7%), and enhanced mixing. Further decreasing $\Delta\rho$ to −0.0071 resulted in the occurrence of the double peaks in the BTCs. The first peak was observed 25% earlier with a 54% lower peak concentration than the BTC at $\Delta\rho = 0$, whereas the second peak was observed 7% earlier with a 63% lower peak concentration.

A similar trend can be observed when only the water flow velocity was decreased at a constant density ratio $\Delta\rho = -0.0036$ (Fig. 3B). The peaks appeared after 0.97, 0.93 and 0.79 pore volumes at the water flow velocities of 1 m d^{-1}, 0.5 m d^{-1} and 0.25 m d^{-1}, respectively. This corresponds to 3%, 7% and 21% earlier appearance of the peak in comparison to the experiment conducted with $\Delta\rho = 0$. Maximum peak concentration decreased from 3.9 mg L^{-1} to 3.2 mg L^{-1} (17% lower) to 2.2 mg L^{-1} (45% lower) with decreasing water flow velocity. Also the experiment C2 ($v = 0.25$ m d^{-1}, $\Delta\rho = -0.0036$) showed the weakly pronounced double peaks.

4.2. Modelling results

Differences in the onset and growth of instabilities between 2D axisymmetric and 3D simulations were found to be consistent for each scenario. Fig. 4A illustrates that the onset of instability fingers in the 2D axisymmetric model started along the left vertical side of the model domain, i.e., the symmetry axis of the column. Then several fingers were developed afterwards, but they merged to form one large finger on the way to the column outflow. In comparison, Fig. 4B shows that the onset of instability fingers in the 3D model was delayed in comparison to 2D axisymmetric, due to dispersion in all directions. Fingers formed evenly over the whole cross section of the model domain and merged together with travel distance. The growth of fingers in 3D was more pronounced than that in 2D axisymmetric, as two fingers with a complex structure persisted over the same travel distance. After 700 min, the front of the 2 mg L^{-1} concentration in 2D is at 0.40 m measured from the bottom, and the front of 2 mg L^{-1} concentration in 3D is at 0.49 m. At the end of the experiment one pronounced finger tended to move along the boundary of the model domain in 3D. A second small finger remained in the centre of the column. In 2D axisymmetric simulations fingers moved always in the centre of the column. This is because recirculation is restricted by the boundaries and the centre of the column was treated as the left boundary of the simulated 2D system.

Fig. 5 shows simulated BTCs from both the 2D axisymmetric and the 3D models with parameters listed in Table 1. Transport is controlled by advection and dispersion in experiments conducted without density contrast (A0, B0, C0). Dispersivity was independent of flow velocity. The tracer breakthrough was in accordance with the applied flow rate. Since transport was linearly coupled with flow, breakthrough curves were easily reproduced by numerical models.

Transport was nonlinearly coupled with flow when density contrast was present. In the experiment A2 ($v = 1.0$ m d^{-1}, $\Delta\rho = -0.0036$), the 2D axisymmetric model yielded a symmetric BTC, indicating no instabilities, as the density effect was dampened by the advection. In the other cases (B2, C2, A4, B4, C4), the 2D axisymmetric model produced asymmetric BTCs, suggesting the formation of instabilities, because the density effect was stronger than the dampening effect of the advection. Negative skewness of the simulated BTCs was observed for the 2D axisymmetric models of B2 ($v = 0.5$ m d^{-1}, $\Delta\rho = -0.0036$) and C2 ($v = 0.25$ m d^{-1}, $\Delta\rho = -0.0036$), with decreasing water flow velocity causing more negative skewness. In contrast to these cases, positive skewness was found for the simulated BTC in the 2D axisymmetric model

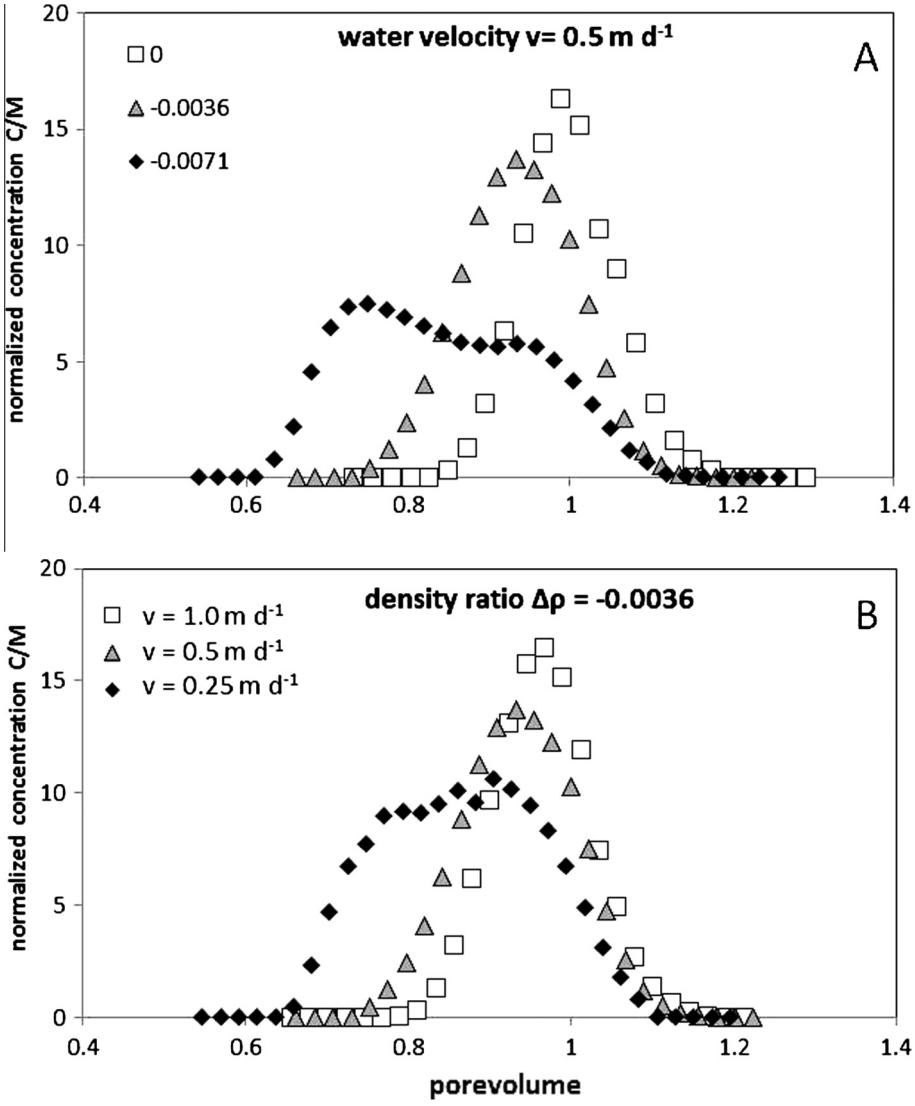

Fig. 3. Observed bromide concentrations for experiments conducted at a water flow velocity of 0.5 m d^{-1} and density ratios of $\Delta\rho = 0$, $\Delta\rho = -0.0036$ and $\Delta\rho = -0.0071$ (A) and observed concentration for a density ratio of $\Delta\rho = -0.0036$ and water flow velocities of 1.0 m d^{-1}, 0.5 m d^{-1} and 0.25 m d^{-1} (B).

of A4 (v = 1 m d^{-1}, $\Delta\rho = -0.0071$). Interestingly, in the 2D axisymmetric model of C4 (v = 0.25 m d^{-1}, $\Delta\rho = -0.0071$), the simulated BTC is negatively skewed. The occurrence of positive and negative skewness of the simulated BTCs from the 2D axisymmetric models resulted from the interplay between complex fingering process and advection. These results are in agreement with the findings obtained by Wood et al. (2004) who conducted column experiments with heavy brines with density ratios ranging from 0.05 to 21.1. Similar BTCs were found for density ratios between 0.05 and 0.9. The results of Wood et al. (2004) further suggest that at higher density ratios (4.8–21.1) BTCs with clearly positive skewness can be expected.

In comparison, Fig. 5 shows that the 3D model produced the identical BTC to the 2D axisymmetric model for the experiment A2 (v = 1 m d^{-1}, $\Delta\rho = -0.0036$). In B2, C2, A4, B4 and C4, transport in the 3D models was influenced by both the density and the flow rate, as observed in the 2D axisymmetric models. However, there are differences in BTCs between 2D axisymmetric and 3D models. The 3D model for the experiment B2 (v = 0.5 m d^{-1}, $\Delta\rho = -0.0036$) produced a symmetric BTC with a lower maximum peak concentration and an earlier breakthrough than the 2D axisymmetric model. The 3D model for the experiment C2 (v = 0.25 m d^{-1}, $\Delta\rho = -0.0036$) produced a highly asymmetric BTC due to the lower pore velocity and the resulting stronger density effect. The breakthrough occurred earlier and the maximum peak concentration was lower than those in the corresponding 2D axisymmetric. Also the 3D model for A4 (v = 1.0 m d^{-1}, $\Delta\rho = -0.0071$) yielded an asymmetrically shaped BTC with weakly pronounced multiple peaks. The occurrence of multiple peaks was attributed to complex shapes of tracer clouds with multiple fingers (Fig. 4B), indicating strong density effect. This was also found in 3D models for B4 (v = 0.5 m d^{-1}, $\Delta\rho = -0.0071$) with BTCs showing multi-peaks and smaller peak concentrations than in 2D axisymmetric. The tracer breakthrough was earlier in 3D than in 2D axisymmetric. C4 (v = 0.25 m d^{-1}, $\Delta\rho = -0.0071$) is the only case where the breakthrough in the 3D was delayed in comparison to the 2D axisymmetric. The peak concentrations in 3D were higher than the ones in the 2D axisymmetric for C4, whereas the peak concentrations were similar or lower in 3D than in 2D in all other scenarios. The different BTCs in 3D were attributed to less restricted dispersion and fingering process and hence stronger interplay between complex fingering process and advection than in 2D.

Fig. 5 also presents relative mass recoveries for both experimental and modelling results. It should be noted that

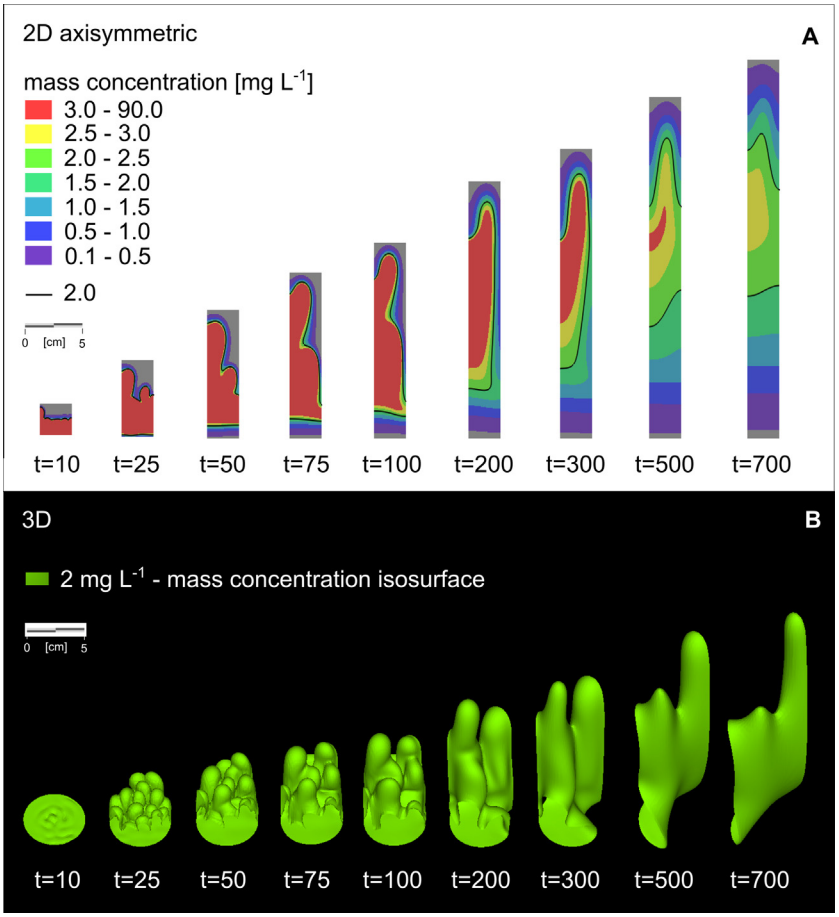

Fig. 4. Visualisation of the onset and growth of instabilities at different time steps in 2D axisymmetric (continuous concentration) and 3D (constant isosurface) performed at the water flow velocity 0.5 m d^{-1} and the density ratio of $\Delta\rho = -0.0071$ (experiment B4).

because of analytical errors, the precision of the final mass recoveries in the experiments was 98 ± 5%. Overall, the mass recovery curves look more stable than the BTCs because of the cumulative nature of these variables. The qualitative inspection suggests that the fitting of the modelled mass recoveries to the measured ones in the 2D axisymmetric models is not significantly different from that in the 3D models, and the fitting of the mass recoveries in both model settings is much better than the fitting of the BTCs. However, in comparison to the BTCs, the mass recoveries were not able to indicate number of fingers, the exit time of those fingers, and hence the degree of instability.

Fig. 6 compares model efficiencies (ME) between the 2D axisymmetric and the 3D models. It can be seen that all the scenarios without density ratios (A0, B0 and C0) resulted in equally high ME (between 98.8% and 99.0%) in both the 2D axisymmetric and the 3D models because of the absence in density effect. When the density ratio was −0.0036, the system became unstable. The ME declined with decreasing water flow velocity in both the 2D axisymmetric (99%, 95% and 93% in A2, B2 and C2 respectively) and the 3D models (99%, 75% and 56% in A2, B2 and C2 respectively). Clearly, this decline trend is more pronounced in 3D than 2D axisymmetric because of less restriction on dispersion. On the contrary, when the density ratio was even higher (−0.0071), the ME increased with decreasing water flow velocity in the 3D case (0.84, 0.87 and 0.85 in A4, B4 and C4 respectively), whereas in the 2D case it decreased first from 0.89 in A4 to 0.75 in B4 followed by the increase to 0.84 in C4. The seemingly conflicting trends between $\Delta\rho$ of −0.0036 and −0.0071 are likely attributed to the relatively high Rayleigh numbers (Table 1). At high Rayleigh numbers, systems become highly transient and chaotic. Hence, the results shown here only represent one possible solution. These trends may change if the models were simulated using different spatial and/or temporal resolutions or noises were added. Prasad and Simmons (2003) and Xie et al. (2012) indicated that highly unstable systems need to be assessed in a stochastic manner rather than a deterministic manner.

Fig. 6 also compares the efficiency in the prediction of the relative mass recovery (MME) between the 2D axisymmetric and the 3D models. Because of the cumulative nature of mass recoveries, the MME was less influenced by variable density flow than the ME. The MME ranged between 97% and 99% in all the 2D axisymmetric models and was consistently higher than the ME. Also the MME ranged between 85% and 99% in all the 3D models and was consistently higher than ME except B4 (ME = 87%, MEE = 95%). All the MME trends for different $\Delta\rho$ are consistent with the ME trends apart from the case of $\Delta\rho = -0.0071$ (A4, B4 and C4). This is because the difference between the modelled and the measured final mass recoveries was apparently smaller in C4 than A4 and B4 as a result of the analytical and the measurement errors (see Fig. 5).

5. Discussion

This study attempted to examine and compare the ability of 2D axisymmetric and 3D numerical models to reproduce variable density flow column experiments, performed at various combinations of water flow velocities and density ratios between the intruding

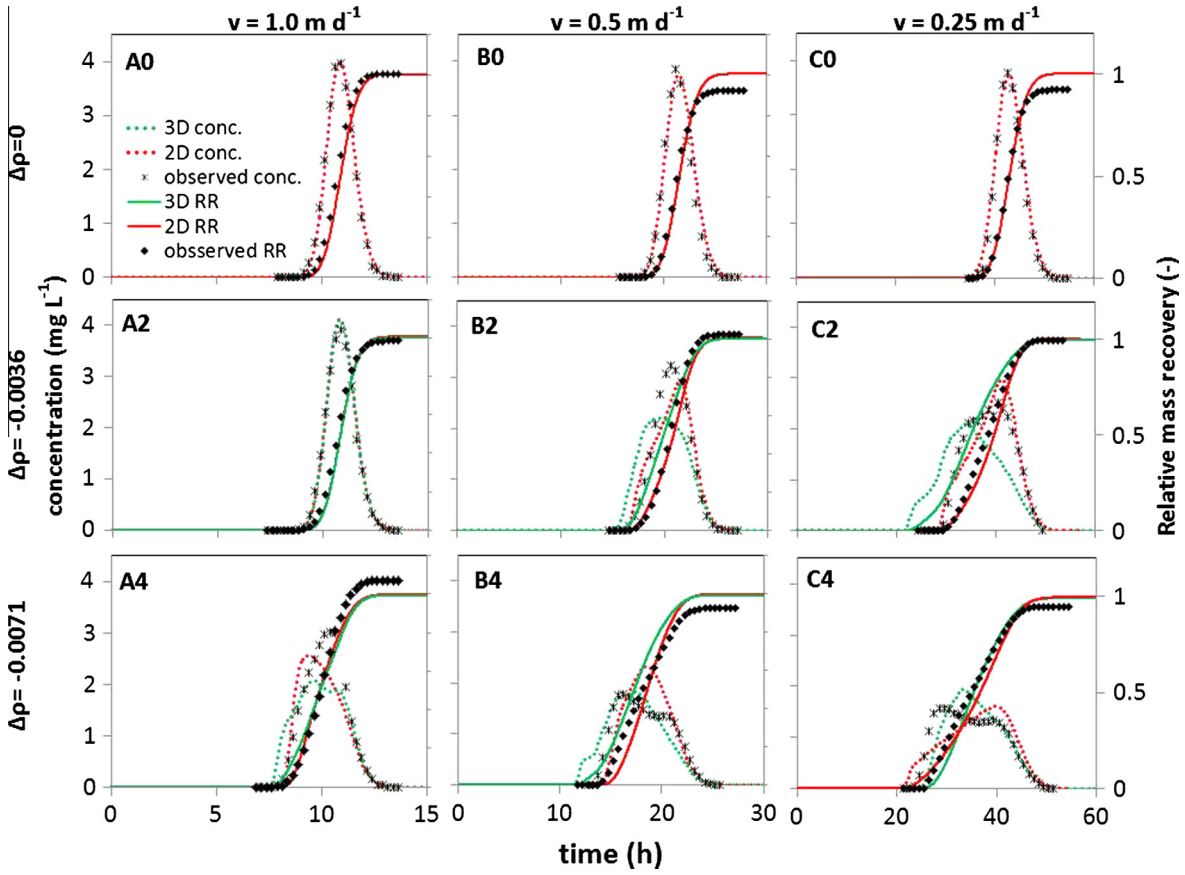

Fig. 5. Comparison of observed and simulated BTCs and relative mass recoveries for nine experiments conducted at three different water flow velocities (A = 1.0 m d^{-1}, B = 0.5 m d^{-1}, C = 0.25 m d^{-1}) and three different density ratios ($\Delta\rho$ = 0 (0), $\Delta\rho$ = −0.0036 (2), $\Delta\rho$ = −0.0071 (4)).

fluid and the ambient fluid. The 2D axisymmetric model represents a vertical cross section of the 3D model. Both models were assessed by comparing finger patterns, concentration breakthrough curves and mass recovery curves to lab experiments.

5.1. Choice of diagnostics

Assessment of the performance of a model is dependent on the choice of diagnostics. The use of BTCs shows that both the 2D axisymmetric and the 3D models are unable to make predictions about the variation in the mean concentration at high density ratios, in particular the timing and the magnitude of the concentration peaks ($\Delta\rho$ = −0.0071 in Fig. 5). This issue has been thoroughly assessed by previous studies (e.g., Johannsen, 2003; Simmons et al., 2001; Xie et al., 2012) through numerical modelling. They concluded that the variable density flow is semi-chaotic and details of this flow process cannot be predicted reliably, because such flows are highly non-linear, non-unique, typically characterised by multiple bifurcation solutions that are triggered and controlled by different numerical features in a numerical model. In some cases, steady solutions may not even exist due to oscillatory regimes (e.g., van Reeuwijk et al., 2009; Johannsen et al., 2006; Diersch, 2013). The simulations conducted in this study represent one possible solution and help to understand the behaviour of density driven tracer plumes in homogeneous sand column experiments. We could run many simulations, introducing "noise" to perturb different solutions each time. One clearly cannot expect to obtain perfect matches of BTCs and fingers in space and time.

In comparison to the BTCs, the models performed better in predicting mass recovery curves, as mass recoveries result from tracer mass integrated over time. This better performance of predicting mass recoveries is indicated by the smaller range of MME than ME in Fig. 6. Thus it is more reasonable to use mass recoveries to assess model performance. The number and positions of simulated instabilities have less influence on mass recovery curves than on the shape of tracer BTCs. Our finding agrees well with previous studies (e.g., Xie et al., 2012) which suggest remarkable reproducibility in the behaviour of macroscopic behaviour.

5.2. Choice of 2D or 3D models

Overall, both ME and MME are greater in the 2D axisymmetric model than those in the corresponding 3D model (Fig. 6). This indicates that a 2D axisymmetric model can be used to make predictions about 3D features of variable density flow as used by numerous prior studies (e.g., Voss and Souza, 1987; Xie et al., 2011, 2012, 2010; Riaz et al., 2006; Jang and Aral, 2007; Prasad and Simmons, 2003, 2005; Dam et al., 2014), and 2D axisymmetric modelling is representative of 3D processes in the longitudinal direction. The predictability could become better using a 2D axisymmetric model when macroscopic diagnostics are used. Hence, 2D axisymmetric modelling is useful and effective to understand penetration speed, transport patterns because of computational efficiency.

Of course, 3D models have the advantage of being able to be used to understand the lateral dispersion/diffusion in the third dimension (e.g., Fig. 4B), because they are obviously much more representative of physical processes in nature, i.e., they do not suppress physics in the third dimension. It is also important to note that although a 2D axisymmetric model attempted to represent

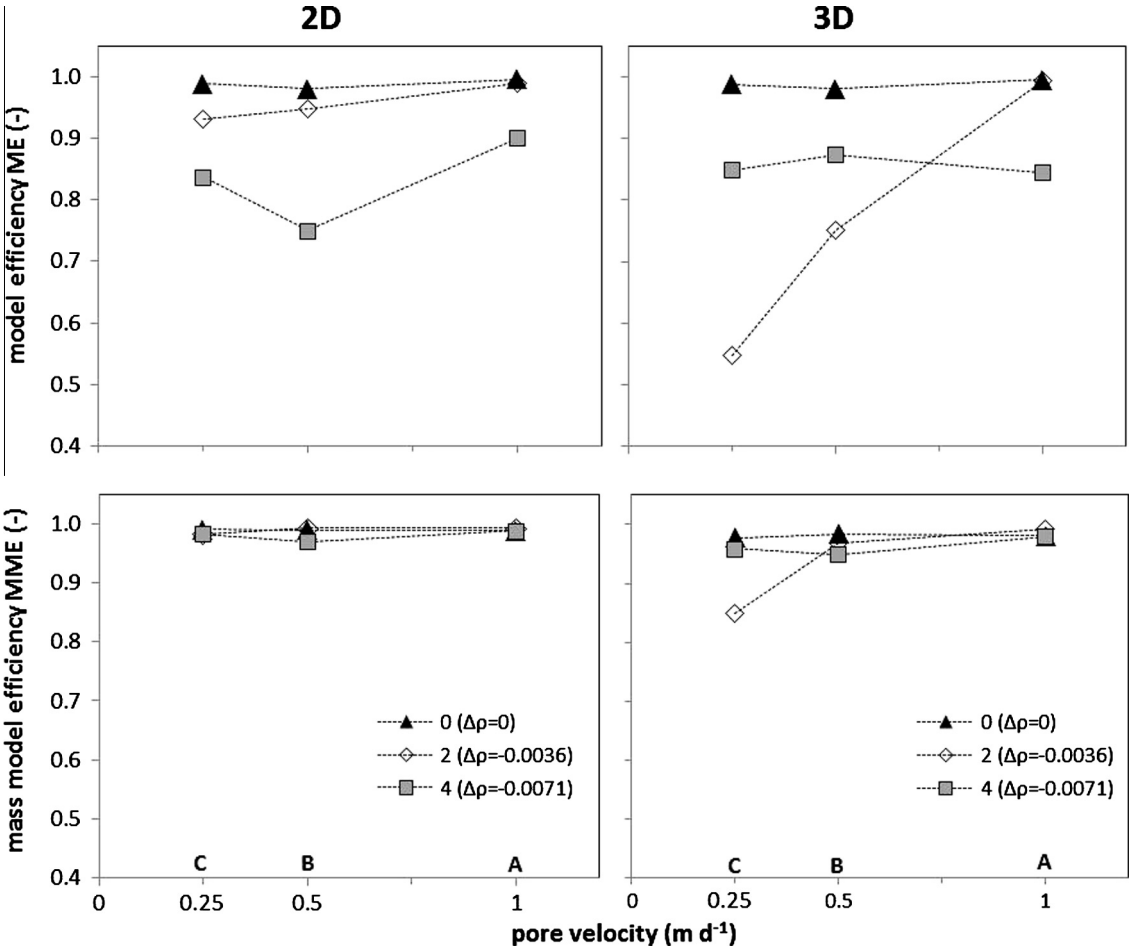

Fig. 6. Model efficiency ME and mass model efficiency MME for reproducing observed concentrations and relative mass recovery in 2D and 3D numerical simulations. A, B and C refer to experiments conducted at water flow velocities of 1, 0.5 and 0.25 m d^{-1}, respectively.

the 3D sand column by changing volumes radially from the column centre, it is still a true 2D model that has restrictions on dimensions and hence flow and transport. Fig. 4 clearly indicates that fingers in the 2D axisymmetric model were restricted to move along the left lateral boundary (i.e., centre of the sand column) which was imposed artificially, whereas fingers in the 3D model were restricted to the true cylindrical boundary.

5.3. Technical difficulties

This study also presents some inherent technical difficulties in assessing variable density flow. The first one relates to the onset of instability. The results suggest that the onset is different between 2D axisymmetric, 3D models and experiments (Figs. 4 and 5). In numerical models, this difference is caused by different numerical errors in 2D axisymmetric and 3D models that act to perturb the unstable boundary layer. In fact, this difference represents a reality of variable density flow in real world. In the experiments, the onset of fingers is induced by the technical design of the column inlet, small-scale heterogeneities in the homogenous sand (caused by packing, grain shape), small variations in pressures caused by the peristaltic pump and the uneven surface of the column wall. All these external influences vary at different times even for the same experiment. All these factors trigger the onset of instabilities but can neither be quantified nor realized in a numerical model. In addition, an exact vertical position of the column is not guaranteed and every deviation would affect the growth and coalescence of fingers. Simmons et al. (2002) conducted sand tank experiments and found many small scale fingers caused by local heterogeneity of pores although relatively homogeneous sand was used. These experimental results were simulated by Cremer and Graf (2015) testing different perturbation methods to reproduce fingers. The pattern of instabilities could be reproduced using a solute source with spatially random, time-constant perturbation.

The second difficulty relates to the computation of mass recoveries. The results suggest that the differences in the total mass recoveries (i.e., final) between the 2D axisymmetric and the 3D models are smaller than between models and experiments (B0, C0, A4, B4 and C4 in Fig. 5). This indicates that properly measuring macroscopic features of variable density flow could be difficult. Our mass recoveries were calculated by integrating measured concentration over time instead of directly measured, because tracer concentration was the only measurable variable. If we can more reliably determine those macroscopic features, numerical models can be better constrained and hence better predictions can be achieved (Prasad and Simmons, 2003; Xie et al., 2012).

5.4. Limitations

This study including both experiments and numerical models assumed that a plume enters a 3D system across the entire inflow area and the whole system is homogeneous and isotropic. In areas such as under salt lakes or landfill sites (e.g., Kimmel and Braids, 1977) or where heterogeneity in hydraulic conductivity prevails (e.g., Post and Simmons, 2010), dense plumes may enter ground-

water through high-permeability areas and can migrate in all directions. Moreover, the spatial distribution of immobile water regions in porous aquifers such as clay lenses, are likely to control the vertical flow pattern of density flow. Consequently, 2D models may not be suitable because dispersion of fluid is limited to a 2D transect, and so 3D models must be used to gain insights into potential migration pathways.

Furthermore, the full extent of fingering processes is restricted by the experimental design, especially by the column wall. The wavelength of instabilities determines if variable density flow is stable or unstable (Schincariol et al., 1994). With increasing Rayleigh number the wavelength for triggering unstable flow becomes smaller (Menand and Woods, 2005). Flowers and Hunt (2007) concluded that unstable variable density flow is only possible when the wavelength of instabilities is smaller than the column diameter. Theoretically, the radius to column height ratio also controls unstable variable density flow under ideal boundary conditions. The critical Rayleigh number triggering instabilities increases with decreasing radius to height ratio (Nield and Bejan, 2012). Clearly, whether and how the column diameter and the radius to column height ratio affect variable density flow needs further investigation.

In this study, viscosity was considered constant throughout the model. This parameter is a function of the properties of liquid components. Adding 4% methanol caused the viscosity to decrease by 11% (Mikhail and Kimel, 1961) and this change should impact on variable density flow. Graf and Boufadel (2011) demonstrated that viscosity could significantly impact the transport of dense plumes. However, this impact can and should be taken into account where parameters such as permeability can be determined precisely. Given permeability measurements could vary by a factor of 3 or more even in laboratory conditions, the effect of viscosity variations are likely negligible compared to variations in permeability.

6. Summary and conclusions

Laboratory experiments have been performed in a homogeneous sand column to examine the effects of spatial dimensionality (2D axisymmetric vs 3D) on variable density flow behaviour. For each experiment, a bromide tracer solution mixed with methanol was injected into a flow field with a constant flow rate. In total, nine experiments were conducted with three different tracer mixtures (variable density) and three different water flow velocities (variable advection). These experiments were then modelled in both 2D axisymmetric and 3D to understand how well 2D axisymmetric models and 3D models could simulate 3D variable density flow processes that occurred in the experiments.

Experimental data indicated the increasing influence of variable density flow on transport with increasing density ratio and decreasing flow rate. This resulted in early breakthroughs of the tracer in comparison to the mean transit time of water. Furthermore, maximum peak concentrations decreased and pronounced double peaks were observed. This highlighted the importance to consider variable density flow even at small density ratios (-0.0036) in transport studies conducted at the laboratory scale. Numerical simulations of experimental results indicated that various fingers were formed in the beginning which merged together with travel distance along the boundary of the model domain. Complex structures of fingers in 3D resulted in highly asymmetric BTCs with pronounced multi peaks. The rather simple shape of fingers obtained in 2D axisymmetric models yielded asymmetric BTCs with a negative skewness. Clearly different BTCs were found for 2D and 3D simulations using the same set of parameters. In both cases, simulations failed to predict details such as the timing and the magnitude of the concentration peaks. Both 2D and 3D models produced high mass recovery efficiency (on average 98% and 95% for 2D axisymmetric and 3D, respectively). The model efficiency in predicting concentrations was lower with 89% for 2D axisymmetric and 81% for 3D. This indicates that the prediction of mass recovery is more reliable than the prediction of concentration at a specific time. Therefore, 2D axisymmetric models can be used to simulate 3D variable density flow in settings such as homogeneous sand columns. Because of less computational demand, 2D modelling is also preferable than 3D when the objective is to quantify macroscopic features such as average finger penetration speed, overall migration behaviour, total solute mass. Certainly, 3D modelling must be performed if we are interested in practical issues such as the spatial scale of dense plume spreading or the likelihood of the occurrence of high solute concentrations.

Acknowledgments

This work was funded by the Helmholtz WasserZentrum München which is part of the SolFlux Platform of the Helmholtz Water Network. Partial support of this work through the HELENA Lab exchange grant is kindly acknowledged.

References

Beinhorn, M., Dietrich, P., Kolditz, O., 2005. 3-D numerical evaluation of density effects on tracer tests. J. Contam. Hydrol. 81 (1–4), 89–105.
Biggar, J., Nielsen, D., 1964. Chloride-36 diffusion during stable and unstable flow through glass beads. Soil Sci. Soc. Am. J. 28 (5), 591–595.
Cremer, C.J., Graf, T., 2015. Generation of dense plume fingers in saturated–unsaturated homogeneous porous media. J. Contam. Hydrol. 173, 69–82.
Dam, R.L., Eustice, B.P., Hyndman, D.W., Wood, W.W., Simmons, C.T., 2014. Electrical imaging and fluid modeling of convective fingering in a shallow water-table aquifer. Water Resour. Res. 50 (2), 954–968.
Diersch, H.-J., 2013. FEFLOW: Finite Element Modeling of Flow, Mass and Heat Transport in Porous and Fractured Media. Springer Science & Business Media.
Diersch, H.J.G., Kolditz, O., 1998. Coupled groundwater flow and transport: 2. Thermohaline and 3D convection systems. Adv. Water Resour. 21 (5), 401–425.
Diersch, H.J.G., Kolditz, O., 2002. Variable-density flow and transport in porous media: approaches and challenges. Adv. Water Resour. 25 (8–12), 899–944.
Flowers, T.C., Hunt, J.R., 2007. Viscous and gravitational contributions to mixing during vertical brine transport in water-saturated porous media. Water Resour. Res. 43 (1).
Flury, M., Flühler, H., 1995. Tracer characteristics of brilliant blue FCF. Soil Sci. Soc. Am. J. 59 (1), 22–27.
Frind, E.O., 1982. Simulation of long-term transient density-dependent transport in groundwater. Adv. Water Resour. 5 (2), 73–88.
Graf, T., Boufadel, M.C., 2011. Effect of viscosity, capillarity and grid spacing on thermal variable-density flow. J. Hydrol. 400 (1–2), 41–57.
Hassanizadeh, S.M., Leijnse, T., 1988. On the modeling of brine transport in porous media. Water Resour. Res. 24 (3), 321–330.
Herbert, A., Jackson, C., Lever, D., 1988. Coupled groundwater flow and solute transport with fluid density strongly dependent upon concentration. Water Resour. Res. 24 (10), 1781–1795.
Hornberger, G.M., Mills, A.L., Herman, J.S., 1992. Bacterial transport in porous media: evaluation of a model using laboratory observations. Water Resour. Res. 28 (3), 915–923.
Huyakorn, P.S., Andersen, P.F., Mercer, J.W., White, H.O., 1987. Saltwater intrusion in aquifers: development and testing of a three-dimensional finite element model. Water Resour. Res. 23 (2), 293–312.
Jang, W., Aral, M.M., 2007. Density-driven transport of volatile organic compounds and its impact on contaminated groundwater plume evolution. Transp. Porous Media 67 (3), 353–374.
Johannsen, K., 2003. On the validity of the Boussinesq approximation for the Elder problem. Comput. Geosci. 7 (3), 169–182.
Johannsen, K., Oswald, S., Held, R., Kinzelbach, W., 2006. Numerical simulation of three-dimensional saltwater-freshwater fingering instabilities observed in a porous medium. Adv. Water Resour. 29 (11), 1690–1704.
Kanel, S.R., Goswami, R.R., Clement, T.P., Barnett, M.O., Zhao, D., 2008. Two dimensional transport characteristics of surface stabilized zero-valent iron nanoparticles in porous media. Environ. Sci. Technol. 42 (3), 896–900.
Kimmel, G.E., Braids, O.C., 1977. Leachate Plumes in Ground Water From Babylon and Islip Landfills. US Geological Survey, Long Island, New York. 2331-1258.
Klute, A., Dirksen, C., 1986. Hydraulic conductivity and diffusivity: laboratory methods. In: Klute, A. (Ed.), Methods of Soil Analysis: Part 1—Physical and Mineralogical Methods. SSSA Book Series. Soil Science Society of America, American Society of Agronomy, pp. 687–734.
Krupp, H.K., Elrick, D.E., 1969. Density effects in miscible displacement experiments. Soil Sci. 107 (5), 372–380.

Levy, B., Chambers, R., 1987. Bromide as a conservative tracer for soil-water studies. Hydrol. Process. 1 (4), 385–389.
Małłoszewski, P., Zuber, A., 1992. On the calibration and validation of mathematical models for the interpretation of tracer experiments in groundwater. Adv. Water Resour. 15 (1), 47–62.
Maloszewski, P., Herrmann, A., Zuber, A., 1999. Interpretation of tracer tests performed in fractured rock of the Lange Bramke basin, Germany. Hydrogeol. J. 7 (2), 209–218.
Maloszewski, P., Zuber, A., 1990. Mathematical modeling of tracer behavior in short-term experiments in fissured rocks. Water Resour. Res. 26 (7), 1517–1528.
Menand, T., Woods, A.W., 2005. Dispersion, scale, and time dependence of mixing zones under gravitationally stable and unstable displacements in porous media. Water Resour. Res. 41 (5).
Mikhail, S.Z., Kimel, W.R., 1961. Densities and viscosities of methanol-water mixtures. J. Chem. Eng. Data 6 (4), 533–537.
Nield, D.A., Bejan, A., 2012. Convection in Porous Media. Springer, New York.
Oostrom, M., Dane, J., Güven, O., Hayworth, J., 1992a. Experimental investigation of dense solute plumes in an unconfined aquifer model. Water Resour. Res. 28 (9), 2315–2326.
Oostrom, M., Hayworth, J., Dane, J., Güven, O., 1992b. Behavior of dense aqueous phase leachate plumes in homogeneous porous media. Water Resour. Res. 28 (8), 2123–2134.
Oswald, S., Kinzelbach, W., Greiner, A., Brix, G., 1997. Observation of flow and transport processes in artificial porous media via magnetic resonance imaging in three dimensions. Geoderma 80 (3–4), 417–429.
Oswald, S.E., Kinzelbach, W., 2004. Three-dimensional physical benchmark experiments to test variable-density flow models. J. Hydrol. 290 (1–2), 22–42.
Pau, G.S.H., Bell, J.B., Pruess, K., Almgren, A.S., Lijewski, M.J., Zhang, K., 2010. High-resolution simulation and characterization of density-driven flow in CO_2 storage in saline aquifers. Adv. Water Resour. 33 (4), 443–455.
Pinder, G.F., Cooper, H.H., 1970. A numerical technique for calculating the transient position of the saltwater front. Water Resour. Res. 6 (3), 875–882.
Post, V.E., Simmons, C.T., 2010. Free convective controls on sequestration of salts into low-permeability strata: insights from sand tank laboratory experiments and numerical modelling. Hydrogeol. J. 18 (1), 39–54.
Prasad, A., Simmons, C.T., 2003. Unstable density-driven flow in heterogeneous porous media: a stochastic study of the Elder 1967b "short heater" problem. Water Resour. Res. 39 (1).
Prasad, A., Simmons, C.T., 2005. Using quantitative indicators to evaluate results from variable-density groundwater flow models. Hydrogeol. J. 13 (5–6), 905–914.
Riaz, A., Hesse, M., Tchelepi, H.A., Orr, F.M., 2006. Onset of convection in a gravitationally unstable diffusive boundary layer in porous media. J. Fluid Mech. 548, 87–111.
Rose, D.A., Passioura, J.B., 1971. Gravity segregation during miscible displacement experiments. Soil Sci. 111 (4), 258–265.
Rühle, F.A., Klier, C., Stumpp, C., 2013. Changes in water flow and solute transport pathways during long-term column experiments. Vadose Zone J. 12 (3).
Schincariol, R.A., Schwartz, F.W., 1990. An experimental investigation of variable density flow and mixing in homogeneous and heterogeneous media. Water Resour. Res. 26 (10), 2317–2329.
Schincariol, R.A., Schwartz, F.W., Mendoza, C.A., 1994. On the generation of instabilities in variable density flow. Water Resour. Res. 30 (4), 913–927.
Simmons, C., 2005. Variable density groundwater flow: from current challenges to future possibilities. Hydrogeol. J. 13 (1), 116–119.
Simmons, C.T., Fenstemaker, T.R., Sharp, J.M., 2001. Variable-density groundwater flow and solute transport in heterogeneous porous media: approaches, resolutions and future challenges. J. Contam. Hydrol. 52 (1–4), 245–275.
Simmons, C.T., Pierini, M.L., Hutson, J.L., 2002. Laboratory investigation of variable-density flow and solute transport in unsaturated-saturated porous media. Transp. Porous Media 47 (2), 215–244.
Van Dam, R.L., Simmons, C.T., Hyndman, D.W., Wood, W.W., 2009. Natural free convection in porous media: first field documentation in groundwater. Geophys. Res. Lett., 36
van Reeuwijk, M., Mathias, S.A., Simmons, C.T., Ward, J.D., 2009. Insights from a pseudospectral approach to the Elder problem. Water Resour. Res. 45 (4).
Voss, C.I., Souza, W.R., 1987. Variable density flow and solute transport simulation of regional aquifers containing a narrow freshwater-saltwater transition zone. Water Resour. Res. 23 (10), 1851–1866.
Wood, M., Simmons, C.T., Hutson, J.L., 2004. A breakthrough curve analysis of unstable density-driven flow and transport in homogeneous porous media. Water Resour. Res. 40 (3).
Xie, Y., Simmons, C.T., Werner, A.D., 2011. Speed of free convective fingering in porous media. Water Resour. Res., 47
Xie, Y., Simmons, C.T., Werner, A.D., Diersch, H.-J.G., 2012. Prediction and uncertainty of free convection phenomena in porous media. Water Resour. Res., 48
Xie, Y., Simmons, C.T., Werner, A.D., Ward, J.D., 2010. Effect of transient solute loading on free convection in porous media. Water Resour. Res., 46
Zheng, C., Bennett, G.D., 1995. Applied Contaminant Transport Modeling: Theory and Practice. Wiley.